Air Plasma-Sprayed Y_2O_3 Coatings for Al_2O_3/Al_2O_3 Ceramic Matrix Composites

This is the authors version of the article published in the

Journal of the European Ceramic Society Vol. 33 (2013) pages 2645–2653

http://dx.doi.org/10.1016/j.jeurceramsoc.2013.03.034

Air Plasma-Sprayed Y_2O_3 Coatings for Al_2O_3/Al_2O_3 Ceramic Matrix Composites

Peter Mechnich*, Wolfgang Braue

German Aerospace Center (DLR), Institute of Materials Research

*Corresponding author. Address: Linder Höhe, 51170 Cologne, Germany

E-mail: peter.mechnich@dlr.de

Phone +49-2203-601-2100; Fax +49-2203-696480;

Abstract

Al_2O_3/Al_2O_3 ceramic matrix composites (CMC) are candidate materials for hot-gas leading components of gas turbines. Since Al_2O_3/Al_2O_3 CMC are prone to hot-corrosion in combustion environments, the development of environmental barrier coatings (EBC) is mandatory. Owing to its favorable chemical stability and thermal properties, Y_2O_3 is considered a candidate EBC material for Al_2O_3/Al_2O_3 CMC. Up to one mm thick Y_2O_3 coatings were deposited by means of air plasma spraying (APS) on Al_2O_3/Al_2O_3 CMC with a reaction-bonded Al_2O_3 bond-coat (RBAO). APS Y_2O_3 coatings exhibit a good adherence in the as-deposited state as well as upon isothermal annealing up to 1400°C. Moreover, furnace cyclic testing performed at 1200°C revealed an excellent durability. This is explained by the formation of a continuous, approximately one micron thick reaction zone at the APS Y_2O_3/RBAO interface. The reaction zone between Y_2O_3 and Al_2O_3 comprises three layers of thermodynamically stable yttrium-aluminates exhibiting strong bonding, respectively.

Keywords: Ceramic Matrix Composites, Al_2O_3/Al_2O_3, Environmental Barrier Coatings, Y_2O_3, Air Plasma Spraying, Yttrium Aluminate.

1. Introduction

Long-term environmental stability is a key issue for the application of oxide/oxide ceramic matrix composites (CMC) in combustion environments of gas turbines. State-of-the-art oxide/oxide CMCs consist of alumina fibers and matrices with submicron grain sizes. At high service temperatures, such Al_2O_3/Al_2O_3 CMC are prone to grain growth, sintering, and creep deformation, resulting in loss of strength and damage tolerance. Moreover, under attack of rapidly flowing, water-vapor rich combustion gases alumina is prone to recession due to formation of volatile species such as $Al(OH)_3$.[1] The application of environmental barrier coatings (EBC) is considered a solution for the degradation problem: EBC separate Al_2O_3-based CMC from rapidly flowing combustion gases and hence promise increased service lifetime and temperature capability of components. EBC materials must be thermodynamically compatible to Al_2O_3, at least at peak service temperature. Low thermal mismatch of CMC and EBC provides minimal thermo-mechanical stresses upon thermal cycling. EBC may also provide additional protection against thermal overload of the Al_2O_3-based CMC.

In recent years, yttrium-silicates (Y_2SiO_5, $Y_2Si_2O_7$) and aluminates (YAG, $Y_3Al_5O_{12}$) gained attention as potential EBC materials exhibiting water-vapor recession rates of two to three orders of magnitude lower than alumina [2,3]. The bulk thermal expansion of Y-silicates (CTE: Y_2SiO_5: 6.9×10^{-6} K^{-1}, $Y_2Si_2O_7$: 4.6×10^{-6} K^{-1} [4]) is low with respect to Al_2O_3 (CTE: Al_2O_3: 9.6×10^{-6} K^{-1}), therefore certain CTE mismatch is anticipated which may affect coating durability. It must be noted that Y-silicates exhibit considerable anisotropic thermal expansion and the CTE mismatch scenario is more complex [5-7]. A more serious issue may be high temperature reactions between EBC materials and Al_2O_3-based CMC: A ternary eutectic exists in the system Al_2O_3-SiO_2-Y_2O_3 having a melting temperature in the 1340-1370°C range [8].

Consequently, for safe operation CMC/EBC interface temperatures must be kept significantly lower than 1340°C. The use of silica-free EBC materials may diminish the reaction problem. For Al_2O_3-based CMC corrosion resistant Y-aluminates such as YAG (yttrium-aluminum-garnet, $Y_3Al_5O_{12}$) are promising. The eutectic temperature of the binary YAG/Al_2O_3 (1826°C [9]) is far beyond realistic application temperatures for Al_2O_3-based CMC. Thermal expansions of YAG (CTE: approx. 9 x 10^{-6} K^{-1}) [10,11] and Al_2O_3 are similar. However, under simulated combustor environments a superficial decomposition of YAG to the Y-enriched phase $Y_4Al_2O_9$ (YAM) and presumably even to pure Y_2O_3 was observed at temperatures above 1350°C.[3] The relative stability of Y_2O_3 with respect to YAG in the combustion environment raises the question whether Y_2O_3 may be a promising TEBC material for Al_2O_3/Al_2O CMC as well. Y_2O_3 is recognized as chemically and thermodynamically very stable material with a melting temperature well beyond 2400°C.[12] Predominantly applications in the nuclear industry are reported in the literature, where Y_2O_3 is used as protection against thermochemical attack by molten metals, slags, etc. [13-15]. Y_2O_3 has a cubic structure (α-Y_2O_3, space-group Ia3).[12] A solid-state phase transformation to a fluorite-type high temperature polymorph (space-group Fm3) is observed above approximately 2200°C [16]. However, this is obviously far beyond plausible CMC operation temperatures. Thermal properties of Y_2O_3 are also very promising for the use as a coating for Al_2O_3-based CMC: thermal expansion data of α-Y_2O_3 published in literature (9.6 x 10^{-6} K^{-1} [12] ; 8.6-9.0 x 10^{-6} K^{-1} [17] ; 8.9 x 10^{-6} K^{-1} [18]) are very close to that of alumina, therefore it is plausible that mechanical stresses induced by CTE mismatch are low. Manufacturing of Y_2O_3 coatings has been performed by a variety of deposition techniques including pulsed laser deposition [19], chemical vapor deposition [20], and, in particular for thick films, air or vacuum plasma-spraying. [21-23] Air plasma spraying (APS) is among the most employed and

investigated technologies for the fabrication of thermal or environmental barrier coatings. [24,25]. Previous work has revealed the benefits of reaction-bonded Al_2O_3 bond-coats (RBAO) for well adhering APS top-coats for porous oxide/oxide CMC. RBAO bond-coats provide uniform, rigid CMC surfaces and sealing of the porous CMC body against gaseous species [26]. In the present work we report on the microstructural development of Al_2O_3/Al_2O_3 CMC with APS Y_2O_3 EBC with special focus on microstructural evolution and phase formation.

2. Experimental procedure

WHIPOX™-type CMC consisting of alumina fibers (Nextel™ 610, 3M) embedded in a porous alumina matrix (Pural, Sasol, Hamburg, Germany) were fabricated at DLR by filament winding. The tubular CMC green body is cut, shaped to a sheet, dried, and sintered (1300°C, one hour). From the sintered CMC plate specimen (120 x 80 x 4 mm) were cut and smoothened by grinding using a 320 mesh SiC paper. Subsequently an approximately 100 μm thick reaction-bonded alumina (RBAO) bond-coat was applied. For this purpose, CMC substrates were painted with an appropriate amount of a Al/Al_2O_3 slurry (70/30 vol%) with isopropanole as dispersant. The Al/Al_2O_3 powder coating converts to a solid RBAO layer upon annealing in air (1300°C, 1 hour). Details of the RBAO coating process as described elsewhere [26]. In a similar manner CMC-tubes with a wall thickness of 4 mm and an inner diameter of 7 mm and were wound, cut to a length of 80 mm, milled to an outer diameter of 13 mm and coated with RBAO. CMC substrates with bond-coats were coated with Y_2O_3 top-coats by air plasma spraying (APS) at the Leibniz University of Hannover (Materials Institute, Department Fortis, Witten, Germany) using an F4 plasma spray gun (Sulzer Metco, Wohlen, Switzerland) and standard spray powders (99.9 % Y_2O_3, -45/+5 μm, Praxair Surface Technologies, Ratingen, Germany). CMC plates were coated with up to 1000 μm thick APS Y_2O_3 whereas coatings of CMC tubes were 200 μm thick. Isothermal heat treatments were carried out in ambient atmosphere using a SiC-heated chamber furnace (HTC 03/15, Nabertherm, Lilienthal, Germany). Thermal cycling was performed in ambient atmosphere using a computer-controlled furnace with vertical arrangement, offering a maximal test temperature of 1200°C.

Phase analysis was performed by X-ray powder diffraction (XRD) (Siemens D5000, CuKα radiation, secondary graphite monochromator, EVA/Topas 4.2 software package, Bruker AXS, Karlsruhe, Germany). Microstructural analyses were

performed by means of scanning electron microscopy (SEM) (DSM Ultra 55, Carl Zeiss NTS, Wetzlar, Germany) with an energy dispersive X-ray spectroscopy (EDS) system (Inca, Oxford Instruments, Abingdon, UK). Supplementary investigations were carried out using focused-ion-beam (FIB) assisted analytical transmission electron microscopy (ATEM) in a Strata 205 FIB system and a Tecnai F30 TEM-STEM with field-emission gun (FEI Inc., Eindhoven, The Netherlands), respectively. Thermal conductivity measurements were carried out by means of laser-flash analysis (LFA 427, Netzsch, Selb, Germany). Vickers hardness of Y_2O_3 coatings was measured with a CLEMEX CMD.HT microhardness tester (Clemex Technologies Inc., Guimond Longueuil, Quebec, Canada).

3. Results

3.1. Properties of as-deposited APS Y_2O_3 and its evolution upon annealing

Figure 1 shows an overview on the 1000 μm thick APS Y_2O_3 coatings deposited on Al_2O_3/Al_2O_3 CMC plates (i) and 200 μm thick coatings on CMC tubes (ii). Coating adhesion is good and cutting of coated CMC specimen could be performed without damaging. Free standing APS Y_2O_3 was employed for determining coating density using the Archimedes method. For this purpose, the CMC substrate was removed by careful grinding, subsequently coating surfaces were polished. Coating density in the as sprayed state was found to be 4.68 g/cm^3, translating to approximately 93 % of the theoretical density of cubic α-Y_2O_3 (5.03 g/cm^3). Figure 2 shows the XRD profile of the as-deposited coating. The dominant phase is α-Y_2O_3 (S.G. Ia3), but weak additional peaks appear in particular in the 25-30° 2-θ range (see close-up in fig. 2). These reflections can unambiguously be assigned to metastable, monoclinic β-Y_2O_3 (S.G. C2/m). Metastable β-Y_2O_3 has been observed in high-pressure or upon rapid solidification of molten submicron particles, e.g. by gas-flame [27, 28] or inductively coupled plasma processing [29]. β-Y_2O_3 has also been found as a constituent phase in air plasma-sprayed Y_2O_3 coatings [22] and is obviously forming upon rapid quenching of deposited Y_2O_3 droplets. On the basis of Rietveld analytical XRD profile fitting it is estimated that 8 wt% of the as-deposited APS Y_2O_3-coating consists of β-Y_2O_3. This concept is supported by SEM analysis of the as-deposited Y_2O_3 coating (fig. 3) revealing that β-Y_2O_3 is mostly found as a small envelope of deposited splats. High magnification SEM imaging (see circular insert in fig. 3) shows remarkable microstructural features: β-Y_2O_3 grains are much smaller than α-Y_2O_3 and exhibit characteristic lamella exhibiting a striking similarity to features observed for

martensitic transformation and twinning of monoclinic ZrO_2. Further, characteristic microstructural features are small cracks arbitrarily running through Y_2O_3 grains.

In order to assess high-temperature microstructural evolution of APS Y_2O_3, specimens were annealed at 1200, 1300, and 1400°C for one hour, respectively (fig 4). Upon annealing metastable β-Y_2O_3 has completed transformed into stable α-Y_2O_3. With respect to Y_2O_3 grain size, the 1200°C and 1300°C samples appear fairly similar. The 1400°C sample, however, shows significant grain growth and polygonization. Starting at 1200°C and even more pronounced at 1300°C, former small intragranular cracks seem to be partially closed and now are transformed into aligned chains of globular pores. At 1400°C, even larger cracks seemingly are closed due to diffusion and sintering, and aligned pores seem to have partially coalesced. Interestingly, after annealing for one hour at 1400°C, the Archimedes measurement yielded an almost identical coating density of 4.69 g/cm^3, i.e. aside from crack closure and pore coalescence, annealing did not produce significant volume effects.

The microstructural changes are reflected also in the average Vickers hardness of the coatings (fig. 5). In the as-deposited state the coatings exhibit an HV50 of 580, which is comparable to the values recently reported for suspension plasma sprayed Y_2O_3 (580-640 HV50). [23] Upon annealing, the hardness increases significantly from 618 (1200°C) up to 672 (1400°C). A closer look at the Vickers indents (fig. 6) reveals that the as-deposited coating (i) exhibits certain plasticity, evidently due to small intragranular cracks providing stress relaxation. On the other hand, the 1400°C annealed coating (ii) clearly exhibits significant embrittlement as indicated by newly formed cracks initiating from the corners of the Vickers pyramid.

Thermal conductivity of APS Y_2O_3 was determined by laser-flash analysis (LFA). For LFA experiments a disc of 13 mm diameter was cut from a free-standing 1mm thick APS coating and subsequently polished to a thickness of 0.425 mm. LFA analysis

was performed by two heating runs from RT to 1400°C with a heating rate of 10 K/min, respectively. At each test temperature (RT, 200-1400°C, 200 K increments) a dwell period of 10 min was kept prior to measurements. Thermal conductivity (λ) of APS Y_2O_3 was calculated from thermal diffusivity on the basis of own density data and Y_2O_3 heat capacity data obtained from literature.[30] Each data point in figure 7 refers to the average value of three individual laser flashes. At a glance, the curves of the first and second heating run show a significant hysteresis, i.e. the second run curve (squares) is running significantly above the first run curve (circles). During the first heating run a minimum of λ is observed around 1000°C and λ is increasing significantly at 1200 and 1400°C. The curve obtained from the second heating run clearly shows that λ has increased significantly by more than 50 % in average. The observations in LFA are easily explained by the microstructural evolution of APS Y_2O_3: the pronounced, sintering-induced closure of cracks and subsequent pore coalescence evidently favors an increasing heat transfer through the coating.

3.2 Evolution of the coating/CMC interface

Figure 8 shows the microstructural evolution of the APS Y_2O_3 / RBAO interface. In the as-deposited state the interface of APS Y_2O_3 and RBAO bond-coat does not show noteworthy features. Most of the RBAO surface seems to be wetted by Y_2O_3, but also small gaps are observed (i). Annealing for one hour at 1200°C produces a layer of tens of nanometers, predominantly at locations where coating and substrate are in close contact (ii). The reaction layer becomes clearly visible upon annealing at 1300°C and now has a thickness of up to 0.5 μm (iii). It is evident that the layer features at least two distinct phases exhibiting different contrast and relief. A further growth of the reaction zone is observed upon annealing at 1400°C (iv). The approximately one μm thick zone features two medium gray contrasted phases

separated by a thin, brightly contrasted phase. This reaction zone extends quasi continuously across the APS Y_2O_3 / RBAO interface. High magnification SEM reveals that all newly formed phases are crystalline, and evidently are yttrium aluminates. An EDS line scan across the reaction zone was performed as indicated by the dotted arrow. In figure 10 the normalized cation content (mol%) is plotted for each of the 60 individual EDS spots. Considering a slight overestimation of yttrium, EDS data indicates that the reaction layer between APS Y_2O_3 and RBAO is featuring all binary equilibrium phases of the system Y_2O_3-Al_2O_3: $Y_4Al_2O_9$ (YAM, theoretically 66.6 mol-% Y), $YAlO_3$ (YAP, 50 mol-% Y) and $Y_3Al_5O_{12}$ (YAG, 37.5 mol-% Y). In order to corroborate this concept, we performed FIB-assisted ATEM with selected area electron diffraction (SAD). For full coverage of the thin reaction layers, in particular intermediate YAP, FIB sectioning was best achieved at glancing incidence with respect to the Y_2O_3/RBAO interface. In the corresponding high-angle angular dark field (HAADF) image (figure 11) the differently contrasted layers of the yttrium aluminates YAG, YAP and YAM are clearly revealed: YAG is enveloping Al_2O_3, YAP is enveloping YAG, and YAM co-exists with YAP. Note that contrast variations within individual layers are due to local thickness variations of the thin foil. Phase analysis along the interface was performed by selected area electron diffraction yielding characteristic zone axis orientation of YAG, YAP and YAM as depicted in figure 12 (i-iii). The assessment of long-term stability of coated CMC is best performed under thermocyclic conditions. In order to avoid preparation artifacts such as edge effects CMC tubes were employed for furnace cyclic testing (FCT). Moreover, it is anticipated that such CMC tubes are well-suited models for “edge-free” components having large curvature radii such as tubular combustor liners. The employed peak temperature of 1200°C is considered a realistic CMC/EBC interface temperature for gas turbine operation. During one cycle the APS Y_2O_3 coated specimen is rapidly

transferred into the 1200°C hot furnace and annealed for a period of 50 min. Then the specimen is rapidly removed from the furnace and cooled down during 10 minutes to room temperature by aid of pressurized air. The FCT campaign was stopped after 500 cycles, i.e. after accumulated 416 hours at 1200°C, since there was no macroscopic evidence of failure such as coating exfoliation or spallation, which is also confirmed by SEM analysis (fig. 13). The APS Y_2O_3 of the FCT sample exhibits a microstructural evolution comparable to the 1h 1400°C sample (see fig. 4). This is also reflected in Vickers hardness measurements, yielding an HV50 of 668 for the FCT sample (see fig.5). A continuous reaction zone has formed at the coating/substrate interface similar to that of the isothermally annealed 1400°C sample.

4. Discussion

The formation of a thermodynamically stable phase assemblage exhibiting strong bonding and low interdiffusion is considered the key issue for the remarkable durability of the Y_2O_3-coating/Al_2O_3-substrate interface. In particular the Y_2O_3-YAM boundary is quasi defect-free, but also the other phases are tightly bound. After the FCT experiment, which is considered a good model for realistic operation conditions, the thickness of the reaction layer is still less than 2 μm, i.e. only a marginal portion of the APS Y_2O_3 coating has been consumed. Assuming a diffusion-controlled reaction, growth of the reaction layer to more than 10 μm, which may be considered as a critical thickness, presumably requires thousands of hours of operation at 1200°C. Interestingly, in parts of the reaction zone of the FCT sample YAM and YAG co-exist without intermediate YAP (fig. 14). This observation can be discussed in the light of previously reported discrepancies with respect to the thermodynamic stability of YAP: Most authors consider YAP to be stable down to room temperature [31] but

some authors report decomposition of YAP to YAM and YAG at temperatures in the 1400-1800°C range [8, and references therein]. Contradictory to such decomposition, YAP has been reported as a product of the reaction between YAG and YAM at temperatures of 1500°C [32]. Our observations seem to support the latter postulation: if the 1200°C FCT sample represents an earlier stage of the YAG+YAM to YAG reaction the 1h 1400°C sample showing a quasi-continuous YAP layer stands for a later reaction stage. Stability issues concerning chemical decomposition are not expected for the other yttrium aluminates up to their congruent melting temperatures (YAG 1942°C, YAM 1977°C), respectively. However, YAM has a monoclinic crystal structure and undergoes a, presumably martensitic, phase transformation at 1377°C [33,34] which may be detrimental for thermocyclic operation. On the other hand, the associated volume change of -0.5 % is relatively small and thus a major detrimental influence on the interface stability is unlikely. Moreover, 1377°C is far beyond a plausible interface temperature, thus a sufficient margin for safe CMC operation is easily maintained.

5. Conclusions

We have investigated the properties and evolution of APS Y_2O_3 coatings deposited on Al_2O_3/Al_2O_3 CMC with porous matrices. RBAO bond-coats provide surface stabilization as well as sealing of porous CMC. APS Y_2O_3 top-coats offer a variety of favorable properties such as a thermal expansion similar to the Al_2O_3-based substrate and low sintering induced shrinkage. A remarkable stability has been observed upon isothermal and thermocyclic treatments. This is explained by a strong chemical bonding between newly formed layers of crystalline yttrium aluminates forming a thin, 1-2 μm thick reaction zone exhibiting high thermodynamic and kinetic stability. Future work will address also the thermocyclic behavior of coated samples having relative small curvature radii, such as standard coupons. For this furnace-cyclic as well as burner-rig tests are envisaged. Up to one mm thick APS Y_2O_3 coatings were successfully deposited on Al_2O_3/Al_2O_3 CMC and it is anticipated that even higher coating thicknesses are achievable. Such thick coatings may provide protection against thermochemical degradation as well as thermal overload; hence may considerably extend the application range of Al_2O_3/Al_2O_3 CMC in combustion environments. A conclusive assessment, however, will require testing in high heat flux and combustion atmosphere, i.e. in a thermal gradient burner rig or in a real turbine engine combustor.

References

[1] Opila EJ, Myers DL. Alumina volatility in water vapour at elevated temperatures. J Am Ceram Soc 2004;**89**:1701-5.

[2] Fritsch M, Klemm H, Herrmann M, Schenk B. Corrosion of selected ceramic materials in hot gas environment. J Eur Ceram Soc 2006;**26**:3557-65.

[3] Fritsch M, Klemm H. The water-vapour hot gas corrosion behavior of Al_2O_3-Y_2O_3 materials, Y_2SiO_5 and $Y_3Al_5O_{12}$-coated alumina in a combustion environment. In: Zhu D, ed. Ceram Eng & Sci Proc 2006;27.3 Hoboken, NJ:Wiley; 2007.

[4] Aparicio R M, Duran A. Yttrium Silicate Coatings for Oxidation Protection of Carbon-Silicon Carbide Composites. J Am Ceram Soc 2000;**83**:1351-55.

[5] Nowok JW, Kay JP, Kulas RJ. Thermal expansion and high-temperature phase transformation of the yttrium silicate Y_2SiO_5. J Mat Res 2001;**16**:2251-55.

[6] Fukuda K, Matsubara H. Anisotropic thermal expansion in yttrium silicate. J Mat Res 2003;**18**:1715-22.

[7] Fukuda K, Matsubara H. Thermal Expansion of δ-Yttrium Disilicate. J Am Ceram Soc 2004;**87**:89-92.

[8] Kolitsch U, Seifert HJ, Ludwig T, Aldinger, F. Phase equilibria and crystal chemistry in the Y_2O_3–Al_2O_3–SiO_2 system. J Mat Res 1999;**14**:447-55.

[9] Nagira, T, Yasuda H, Yoshiya, M. Formation and microstructure of Al_2O_3-YAG eutectic ceramics by phase transformation from metastable system to equilibrium system. J of Physics:Conference Series 2009;**165**:012006.

[10] Gupta TK, Valentich, J. Thermal Expansion of Yttrium Aluminum Garnet. J Am Ceram Soc 1971;**54**:355-56.

[11] Cao XQ, Vassen R, Stoever, D. Ceramic materials for thermal barrier coatings. J Eur Ceram Soc 2004;**24**:1-10.

[12] Curtis CE. Properties of Yttrium Oxide Ceramics. J Am Ceram Soc 1957;**40**:274-78.

[13] Terai T. Research and Development on Ceramic Coatings for Fusion Reactor Liquid Blankets. J Nucl Mat 1997;**248**:153-58.

[14] Nagaraj A, Anupama P, Mukherjee J, Sreekumar KP, Satpute RU, Padmanabhan PVA, Gantayet LM. Thermal stability studies of plasma sprayed yttrium oxide coatings deposited on pure tantalum substrate. J of Physics: Conference Series 2010; **208**:012124.

[15] Alangi N, Mukherjee J, Anupama P, Verma MK, Chakravarthy Y, Padmanabhan PVA, Das AK, Gantayet LM. Liquid uranium corrosion studies of protective yttria coatings on tantalum substrate. J Nucl Mat 2011;**420**:39-45.

[16] Swamy V, Dubrovinskaya NA, Dubrovinsky LS. High-temperature powder x-ray diffraction of yttria to melting point. J Mat Res 1999;**14**:456-59.

[17] Nielsen TH, Leipold MH. Thermal Expansion of Yttrium Oxide and of Magnesium Oxide with Yttrium Oxide. J Am Ceram Soc 1964;**47**:256.

[18] Stecura S, Campbell WJ. Thermal expansion and phase inversion of rare-earth oxides. Report of investigations no. 5847. Washington: Bureau of Mines; 1961.

[19] Singh AK, Kutty TRG, Sinha S. Pulsed laser deposition of corrosion protective Yttrium Oxide (Y_2O_3) coating. J Nucl Mat 2012;**420**:374-81.

[20] Goto T, Banal R, Kimura T. Morphology and preferred orientation of Y_2O_3 film prepared by high-speed laser CVD. Surf Coat Techn 2007;**201**:5776-81.

[21] Berkowski M, Bowen P, Liechti T, Scheel HJ. Plasma-Sprayed-Yttria Layers for Corrosion Resistance. J Am Ceram Soc 1992;**75**:1005-7.

[22] Gourlaouen V, Schnedecker G, Lejus AM, Boncoeur M, Collongues R. Metastable Phases in Yttrium Oxide Plasma Spray Deposits and their Effect on Coating Properties. Mat Res Bull 1993;**28**:415-25.

[23] Kitamura J, Tang Z, Mizuno H, Sato K, Burgess A. Structural, Mechanical and Erosion Properties of Yttrium Oxide Coatings by Axial Suspension Plasma Spraying for Electronics Applications. J Therm Spray Techn 2011;**20:**170-86.

[24] Lee KN, Fox DS, Bansal NP. Rare earth silicate environmental barrier coatings for SiC/SiC composites and Si_3N_4 ceramics. J Eur Ceram Soc 2005;**25**:1705-15.

[25] Weyant CM, Faber KT. Processing–microstructure relationships for plasma-sprayed yttrium aluminum garnet. Surf Coat Techn 2008;**202**:6081–89.

[26] Mechnich P, Braue W, Schneider H. Multifunctional reaction-bonded alumina coatings for porous continuous fiber-reinforced oxide composites. Int J Appl Ceram Techn 2004;**1**:343-50.

[27] Guo B, Harvey A, Risbud SH, Kennedy IM. The formation of cubic and monoclinic Y_2O_3 nanoparticles in a gas-phase flame process. Phil Mag Lett 2006;**86**:457-67.

[28] Guo B, Mukundan M, Yim H. Flame aerosol synthesis of phase-pure monoclinic Y_2O_3 particles via particle size control. Powder Technoloy 2009;**191**:231-34.

[29] Vogt GJ. Synthesis of the monoclinic yttria by thermal plasma processing. 172.Meeting of the Electrochemical Society, Honolulu, HI, USA. Los Alamos National Library LA-UR--87-3149; 1987.

[30] Swamy V, Seifert HJ, Aldinger F. Thermodynamic properties of Y_2O_3 phases and the yttrium–oxygen phase diagram. J Alloys Comp 1998;**269**:201-7.

[31] Medraj M, Hammond R, Parvez MA, Drew RAL, Thomson WT. High temperature neutron diffraction study of the Al_2O_3–Y_2O_3 system. J Eur Ceram Soc 2006;**26**:3515-24.

[32] Lo JR, Tseng TY. Phase development and activation energy of the Y_2O_3-Al_2O_3 system by a modified sol-gel process. Mat Chem Phys 1998;**56**:56-62.

[33] Yamane H, Omori M, Okubo A, Hirai T. High-Temperature Phase Transition of $Y_4Al_2O_9$. J Am Ceram Soc 1993;**76**:2382-84.

[34] Yamane H, Ogawara K, Omori M, Hirai T. Therrmal Expansion and Thermal Phase Transition of $Y_4Al_2O_9$ Ceramics. J Am Ceram Soc 1995;**78**:1230-32.

Figure Captions

Fig. 1: Microstructure of 1000 mm APS Y_2O_3 coating on Al_2O_3/Al_2O_3 CMC plate (i) and 200 mm APS Y_2O_3 on Al_2O_3/Al_2O_3 CMC tube (ii). Coatings exhibit good adherence irrespective of thickness and substrate shape.

Fig. 2: XRD profile of as-deposited APS Y_2O_3 coating. The major peaks refer to cubic α-Y_2O_3, but metastable, monoclinic β-Y_2O_3 co-exists (see 25-35° close-up). Rietveld analysis yields an estimate of 8 wt% β-Y_2O_3.

Fig. 3: SEM of as-deposited APS Y_2O_3 coating. The dominant phase is cubic α-Y_2O_3, small monoclinic β-Y_2O_3 grains are typically located at splat boundaries. The close-up reveals that β-Y_2O_3 exhibits characteristic lamellae which probably are due to twinning.

Fig. 4: SEM of APS Y_2O_3 coatings upon annealing (1 h). Whereas grain sizes do not change at 1200°C and 1300°C, grain growth is evident at 1400°C. Progressive crack closure and pore coalescence are evident.

Fig. 5: Effect of annealing on APS Y_2O_3 Vickers microhardness.

Fig. 6: SEM images of Vickers indents of as-deposited and annealed (1400°C, 1 h) APS Y_2O_3. Indents as well as crack morphology are indicative for thermally induced coating embrittlement.

Fig. 7: Thermal conductivity (λ) of APS Y_2O_3 coatings determined by laser-flash analysis (LFA). Circles refer to data from first heating run, squares to the second run. In the first run, increase of λ above 1000°C marks onset for sintering. Due to sintering-induced closure of microcracks significant higher values for λ are observed in the second run.

Fig. 8: SEM images of the APS Y_2O_3/RBAO interface in the as-deposited state (i) and upon different one hour annealings (ii-iv). A reaction layer comprising differently contrasted phases is growing at the interface.

Fig. 9: SEM close-up of the APS Y_2O_3/RBAO interface upon one hour annealing at 1400°C. The reaction zone comprises three layers of crystalline phases. An EDS line scan (dotted arrow) was performed across the reaction zone (see also fig. 10).

Fig. 10: Quantitative EDS line scan across the APS Y_2O_3/RBAO interface (see fig. 9). Taking into account a slight over-estimation of Y, each layer of the reaction zone can be assigned to an equilibrium phase of the Al_2O_3-Y_2O_3 system.

Fig. 11: STEM dark field (HAADF) image of the Y_2O_3/RBAO interface upon a one hour anneal at 1400°C (FIB section taken at glancing incidence relative to the interface)

Fig. 12: Electron diffraction zone axis patterns of interfacial constituents from the α-Y_2O_3/RBAO interface upon one hour annealing at 1400°C: (i) cubic YAG; (ii) orthorhombic YAP; (iii) monoclinic YAM.

Fig. 13: SEM overview of the APS Y_2O_3/RBAO interface upon FCT (500 one hour cycles at 1200°C). The continuous reaction zone exhibits a striking similarity to the 1 h/1400°C sample (see also fig. 9).

Fig. 14: SEM close-up of the APS Y_2O_3/RBAO interface upon FCT (500 one hour cycles at 1200°C). Note that the YAP ($YAlO_3$) layer between YAM ($Y_4Al_2O_9$) and YAG ($Y_3Al_5O_{12}$) is discontinuous.

Figure 1

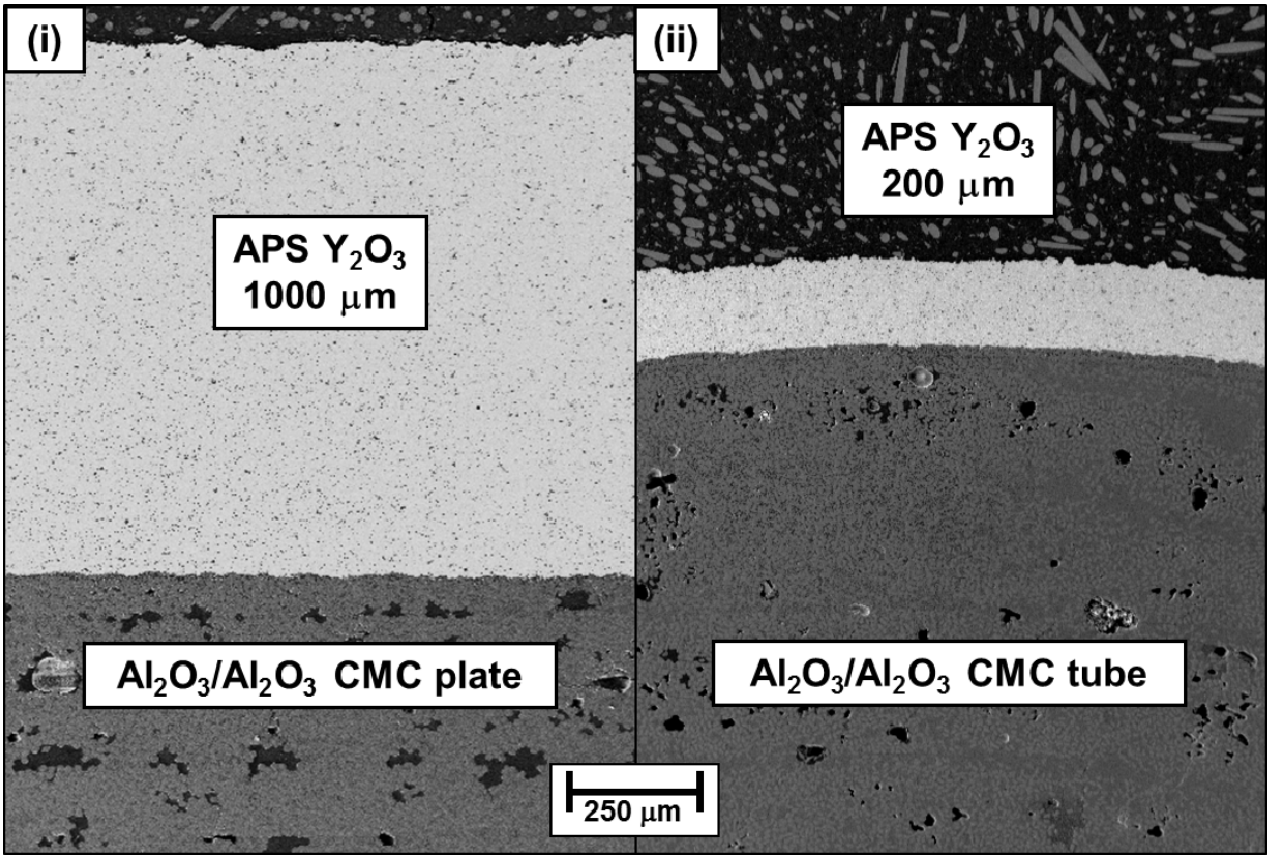
(i)
APS Y_2O_3
1000 μm
Al_2O_3/Al_2O_3 CMC plate
(ii)
APS Y_2O_3
200 μm
Al_2O_3/Al_2O_3 CMC tube
250 μm

Figure 2

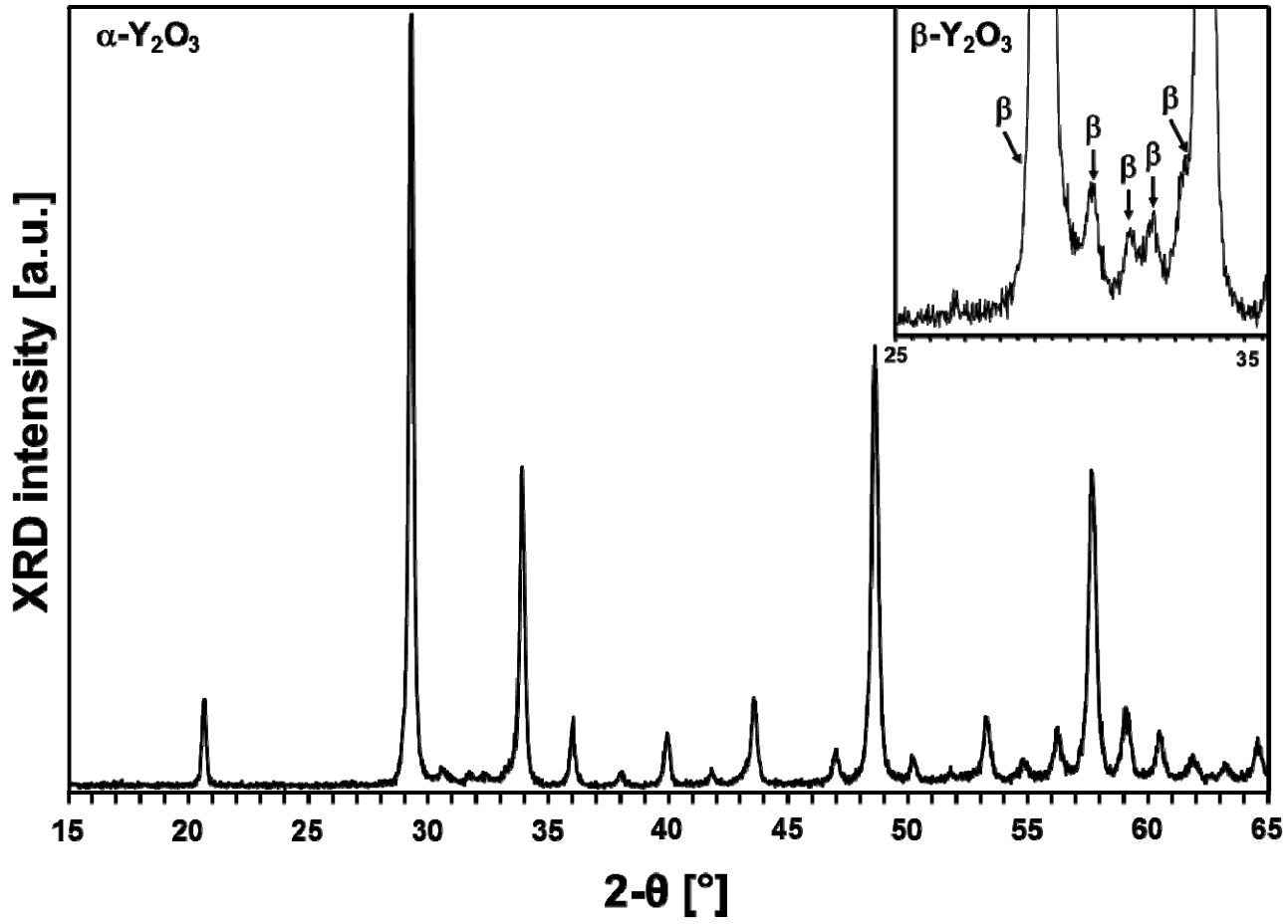
α-Y2O3
β-Y2O3
β
β
β
β
β
25
35
XRD intensity [a.u.]
15
20
25
30
35
40
45
50
55
60
65
2-θ [°]

Figure 3

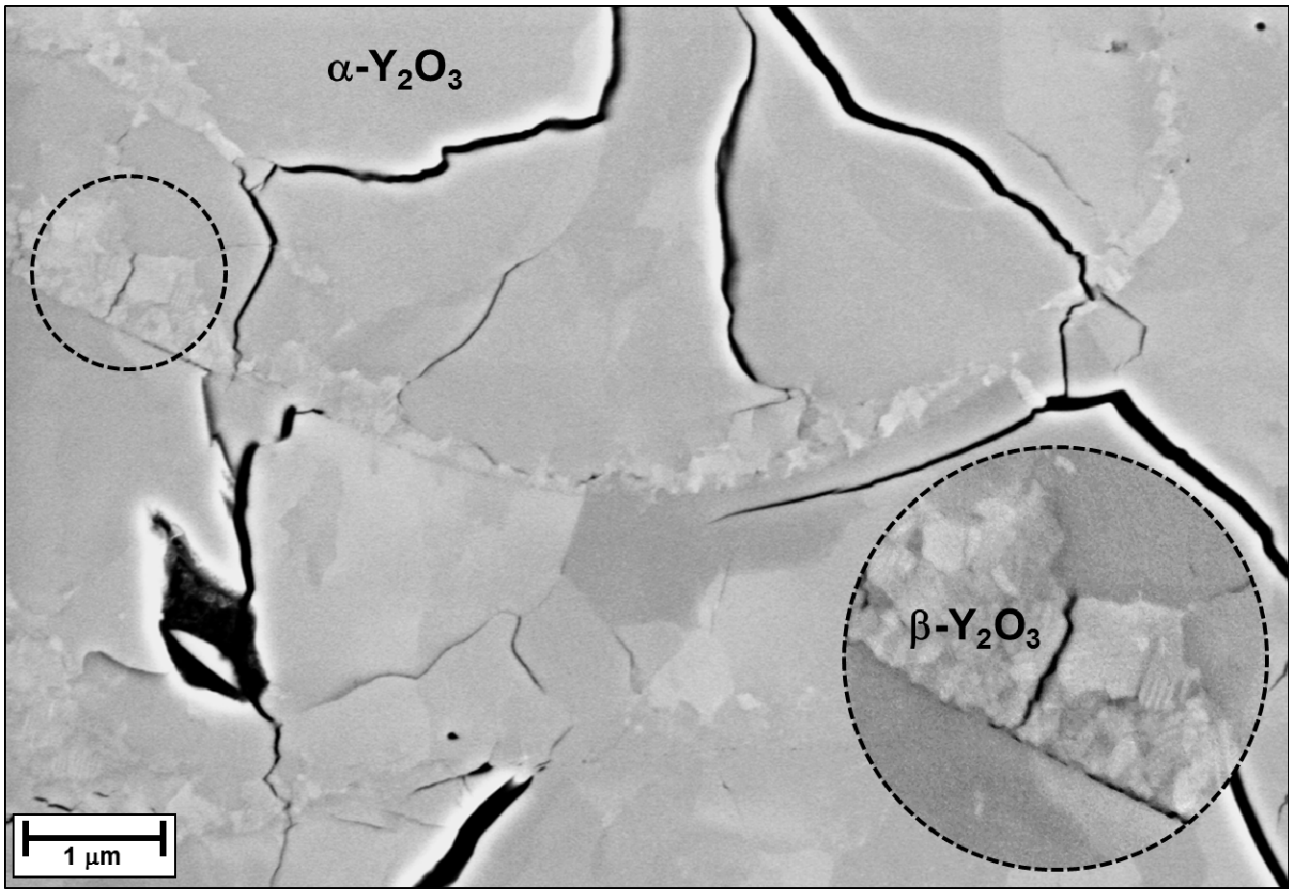

Figure 4

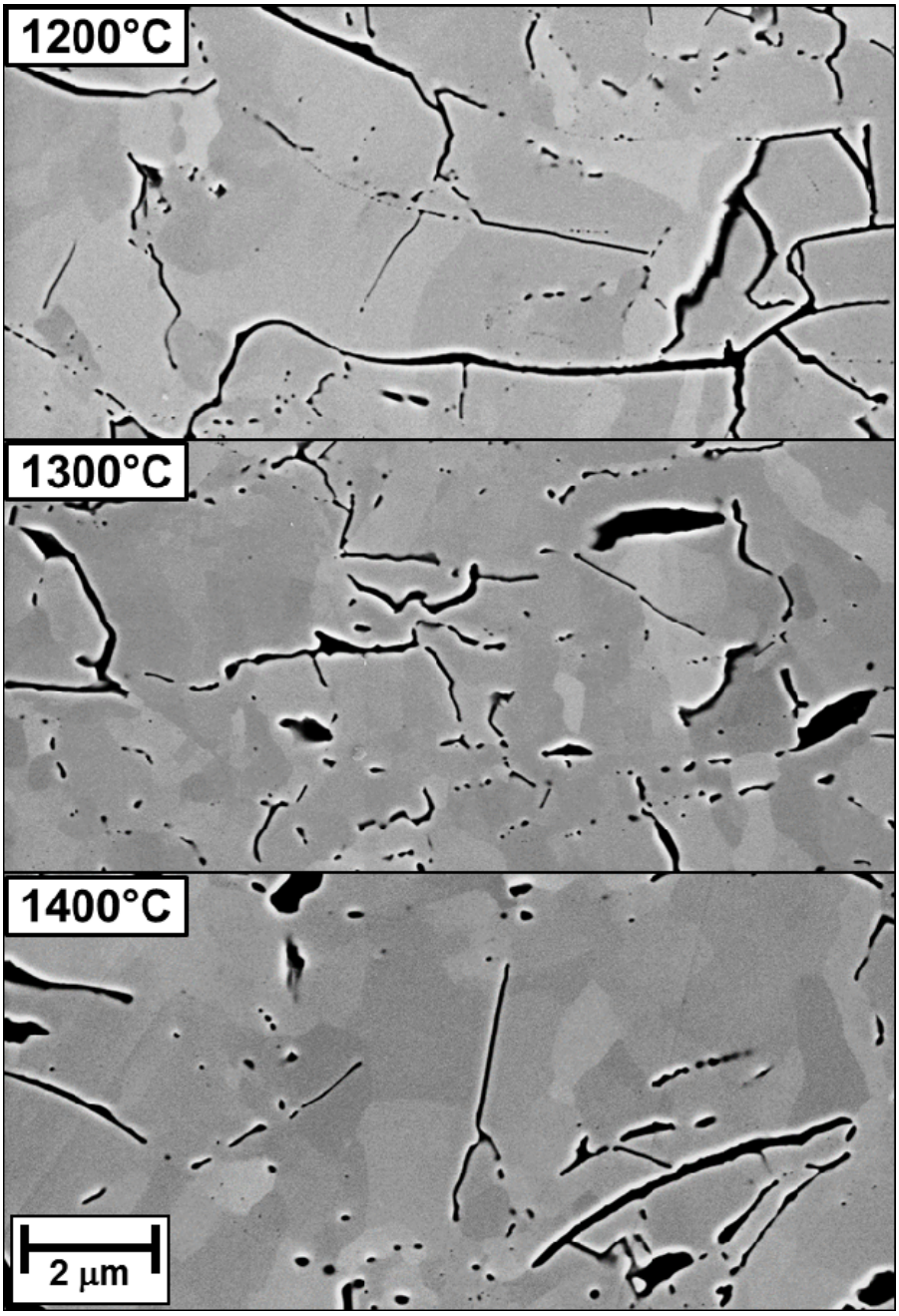

Figure 5

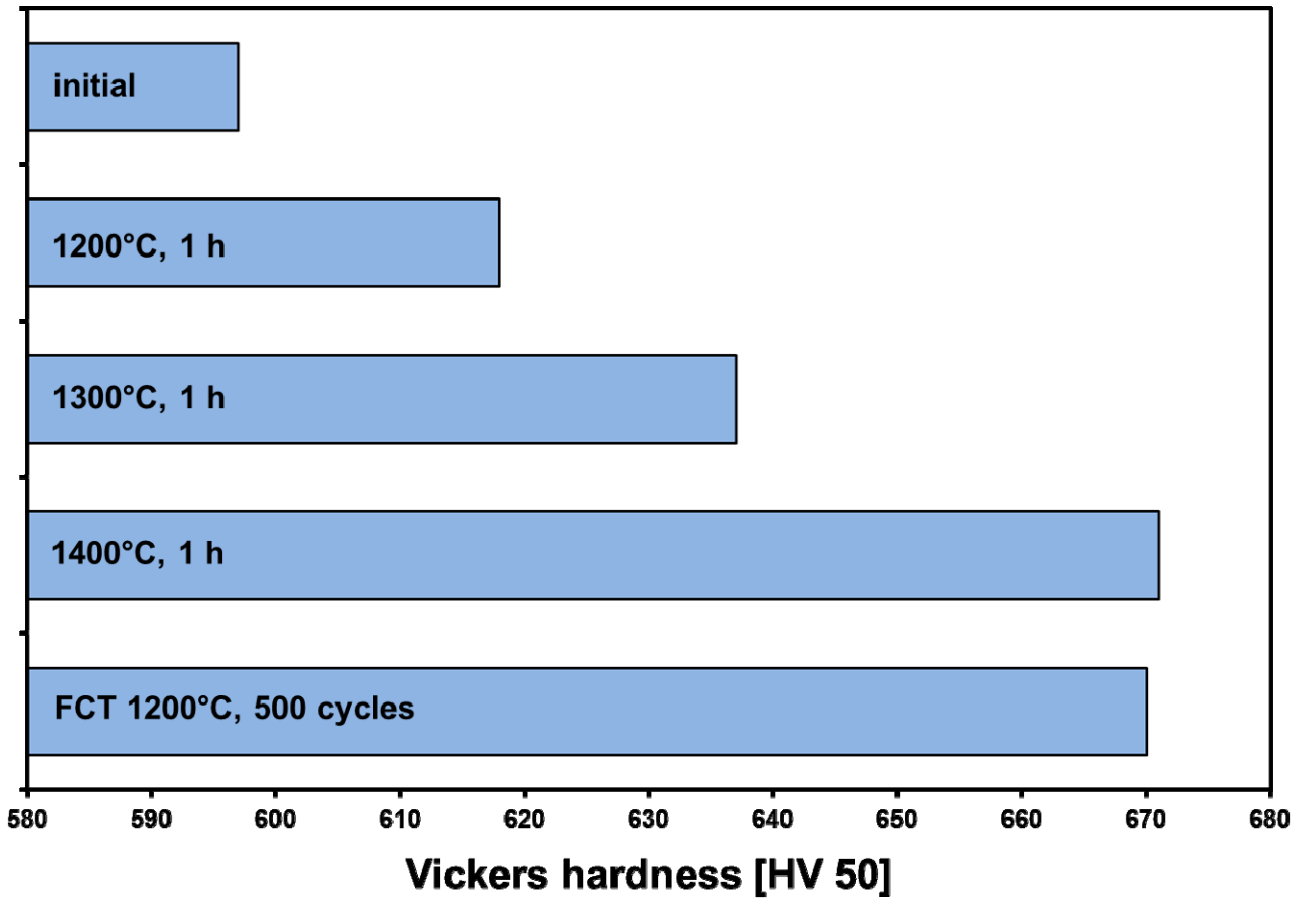
initial
1200°C, 1 h
1300°C, 1 h
1400°C, 1 h
FCT 1200°C, 500 cycles
580
590
600
610
620
630
640
650
660
670
680
Vickers hardness [HV 50]

Figure 6

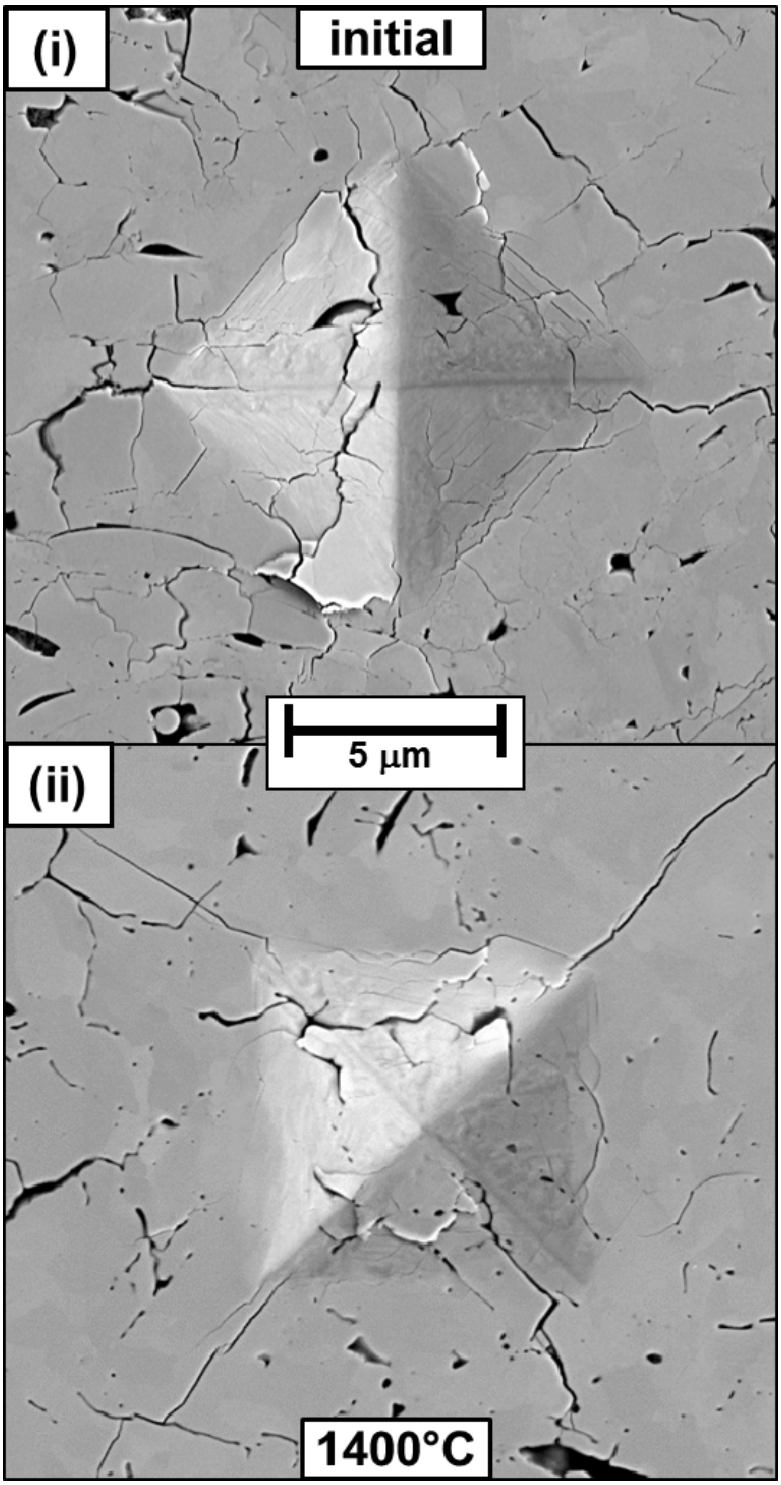

Figure 7

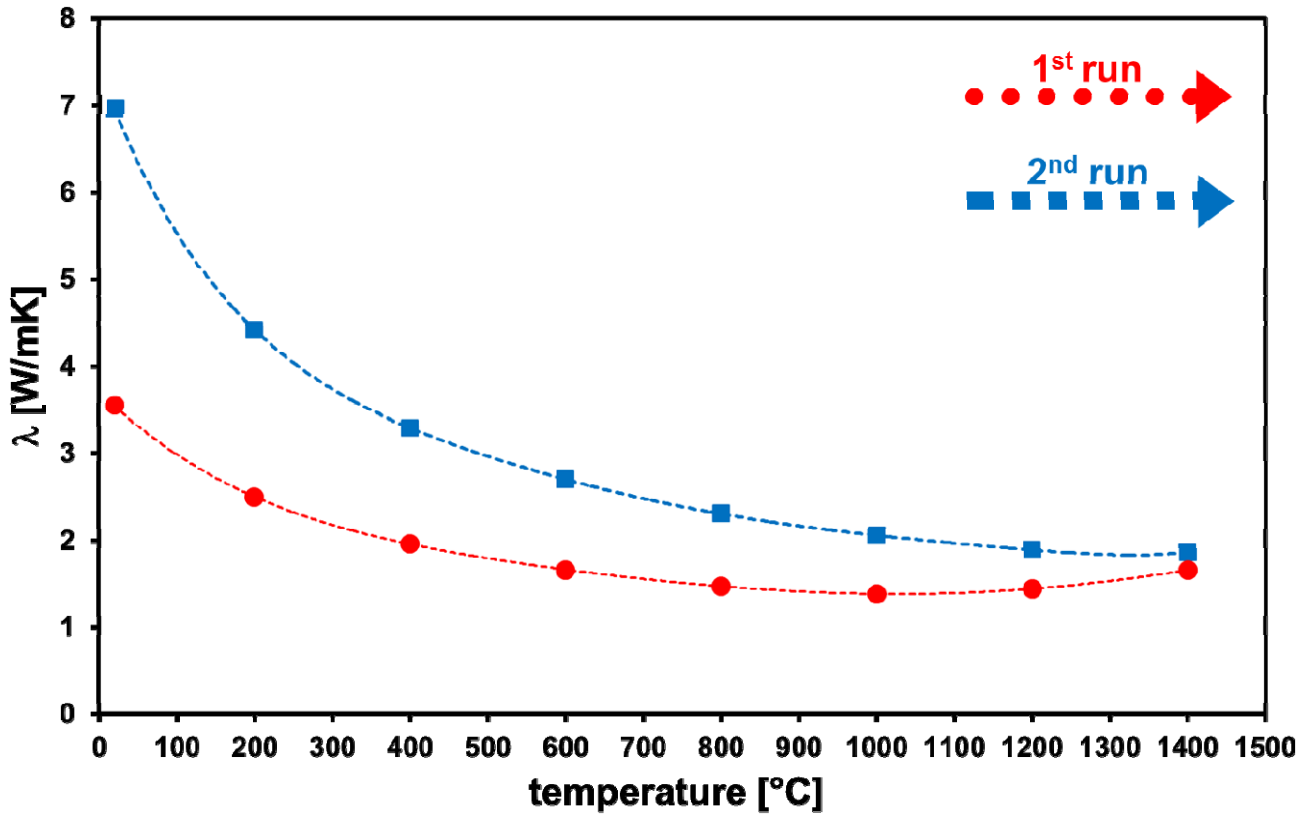
λ [W/mK]
temperature [°C]
1st run
2nd run
0
1
2
3
4
5
6
7
8
0
100
200
300
400
500
600
700
800
900
1000
1100
1200
1300
1400
1500

Figure 8

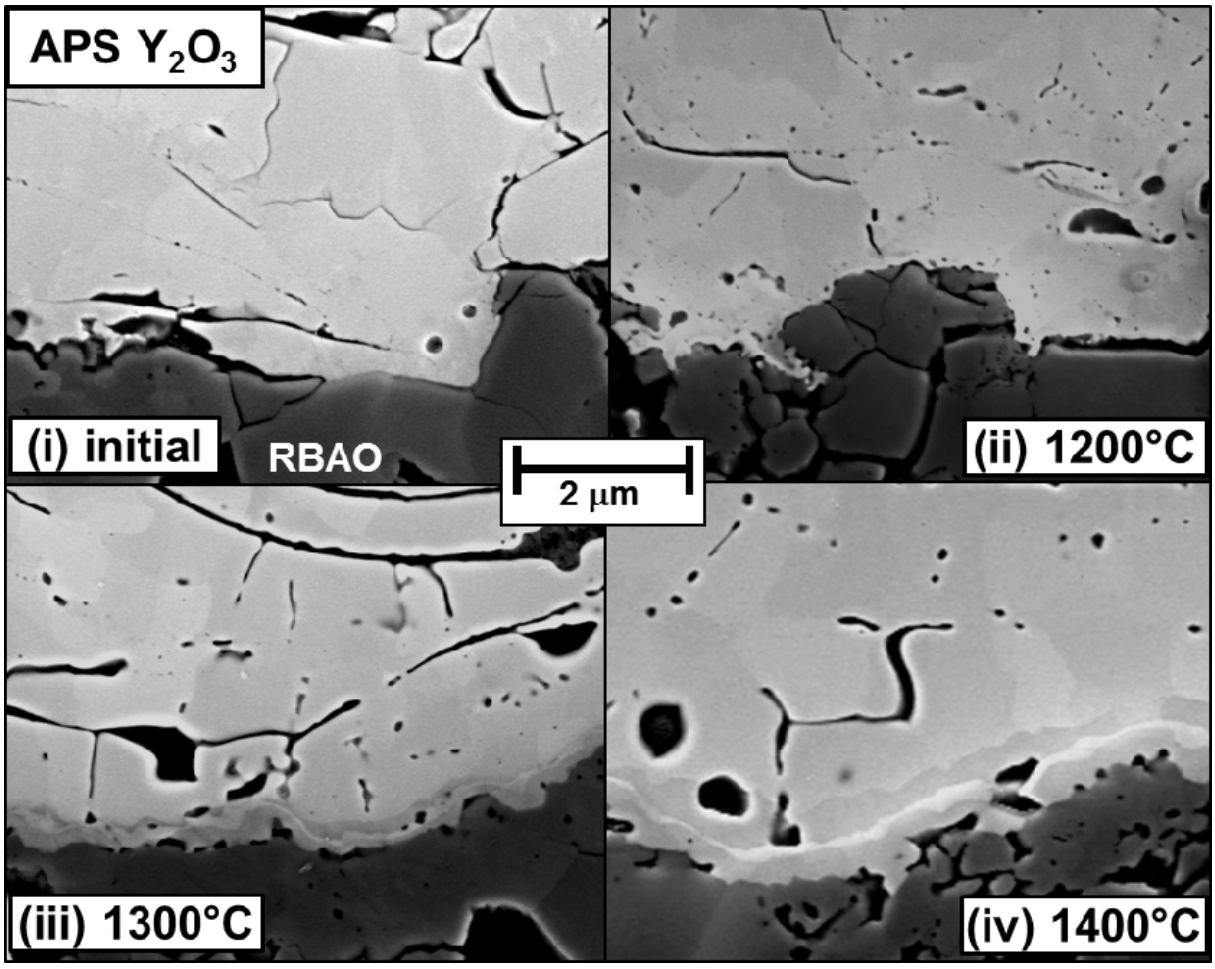

Figure 9

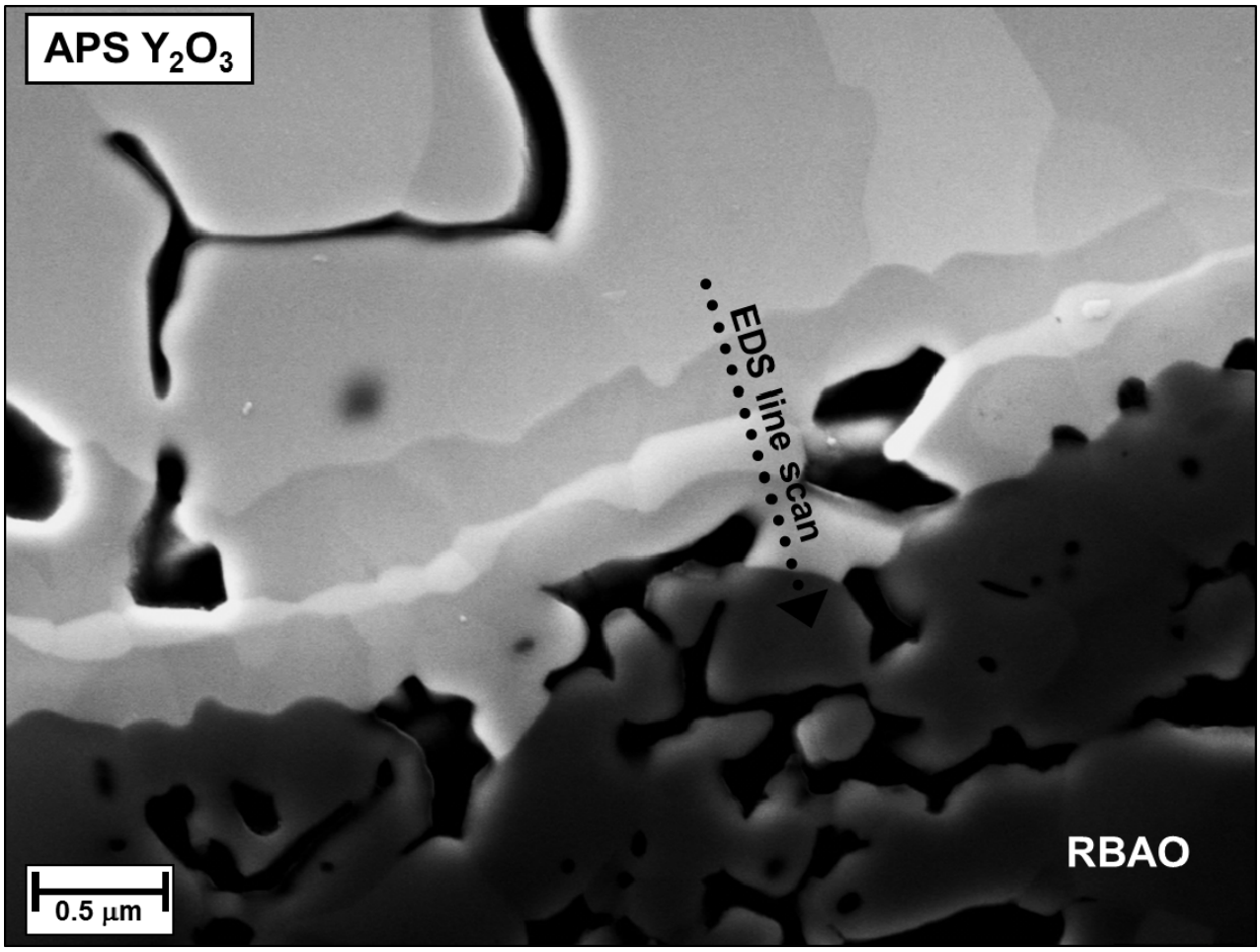

Figure 10

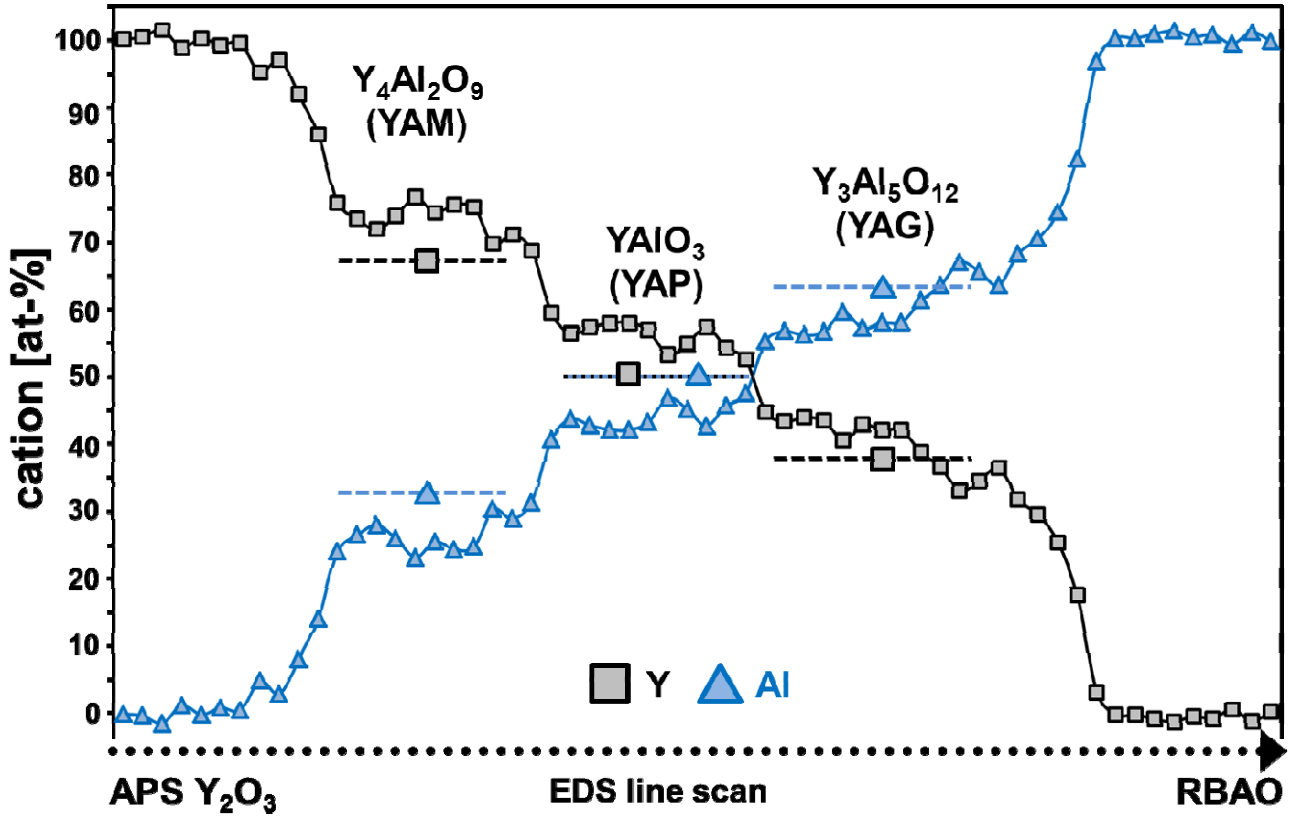
cation [at-%]
100
90
80
70
60
50
40
30
20
10
0
$Y_4Al_2O_9$
(YAM)
$YAlO_3$
(YAP)
$Y_3Al_5O_{12}$
(YAG)
Y
Al
APS Y_2O_3
EDS line scan
RBAO

Figure 11

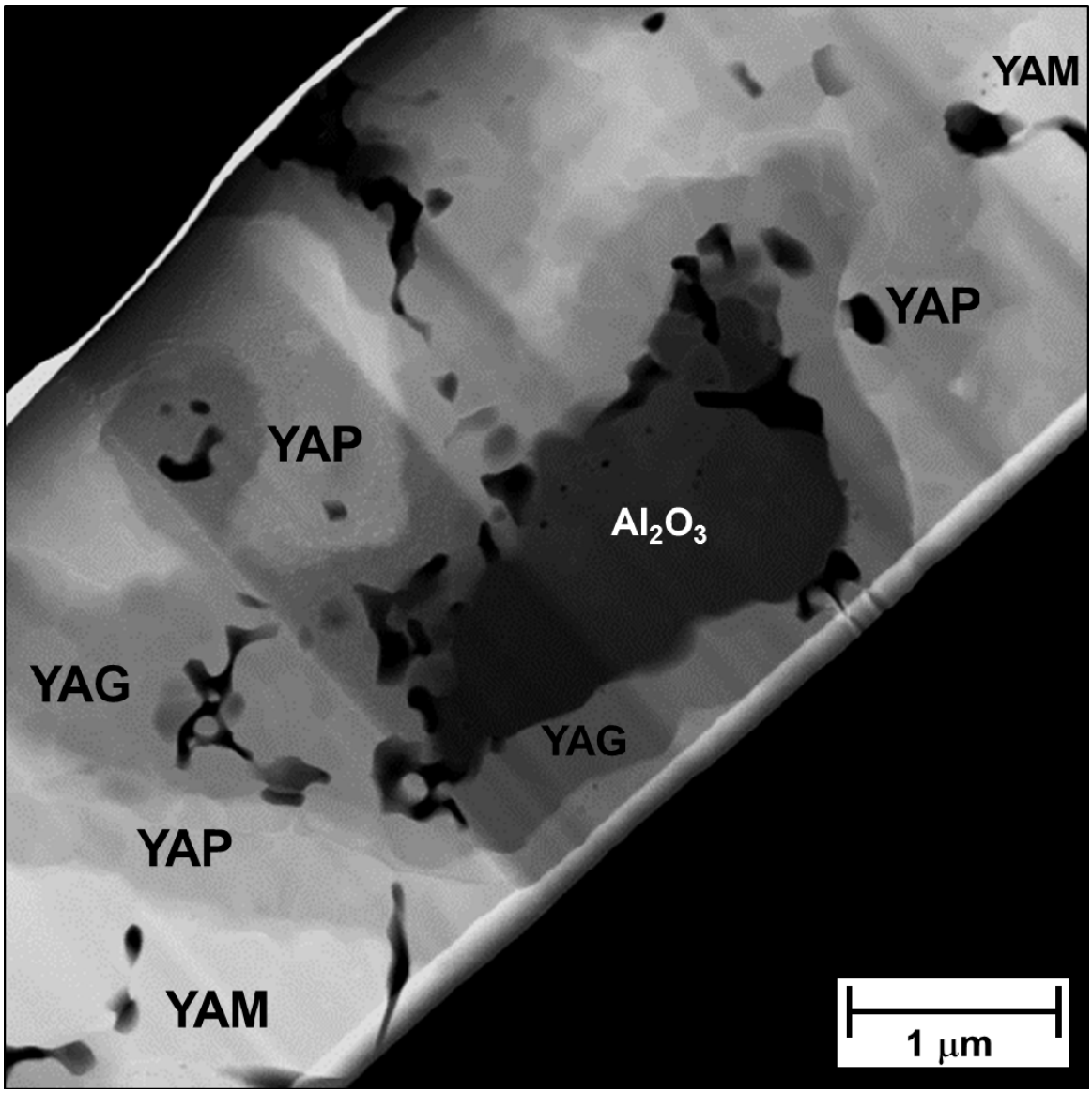

Figure 12

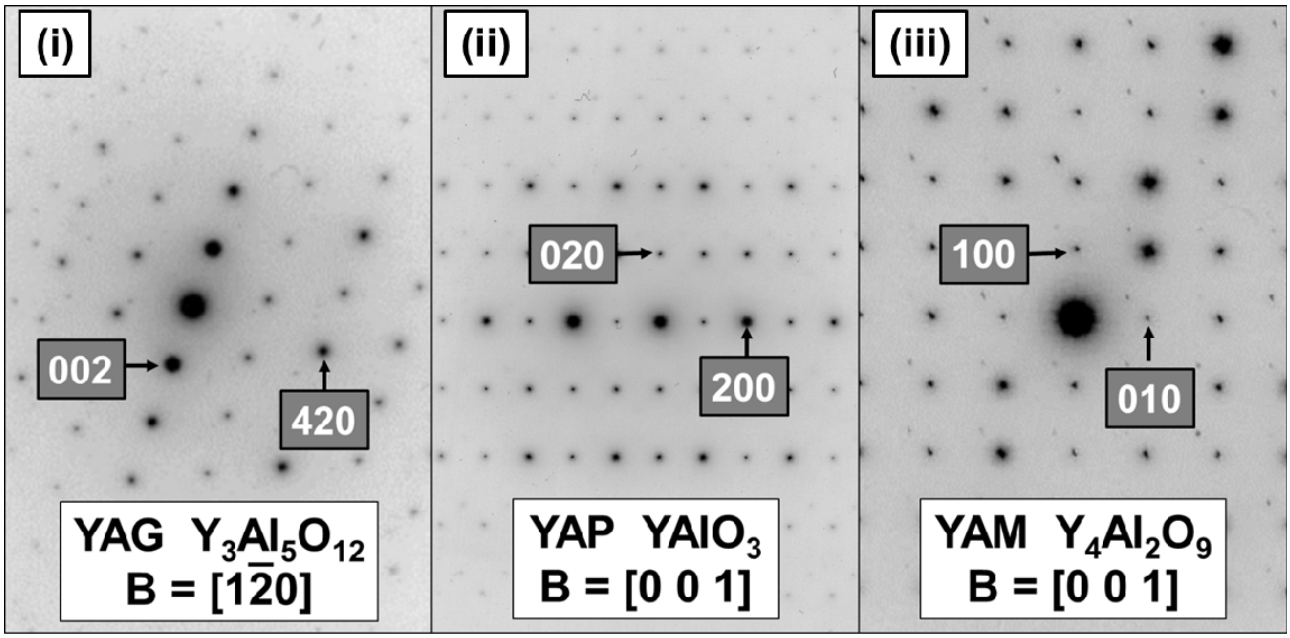
(i)
002
420
YAG $Y_3Al_5O_{12}$
B = [1$\bar{2}$0]
(ii)
020
200
YAP $YAlO_3$
B = [0 0 1]
(iii)
100
010
YAM $Y_4Al_2O_9$
B = [0 0 1]

Figure 13

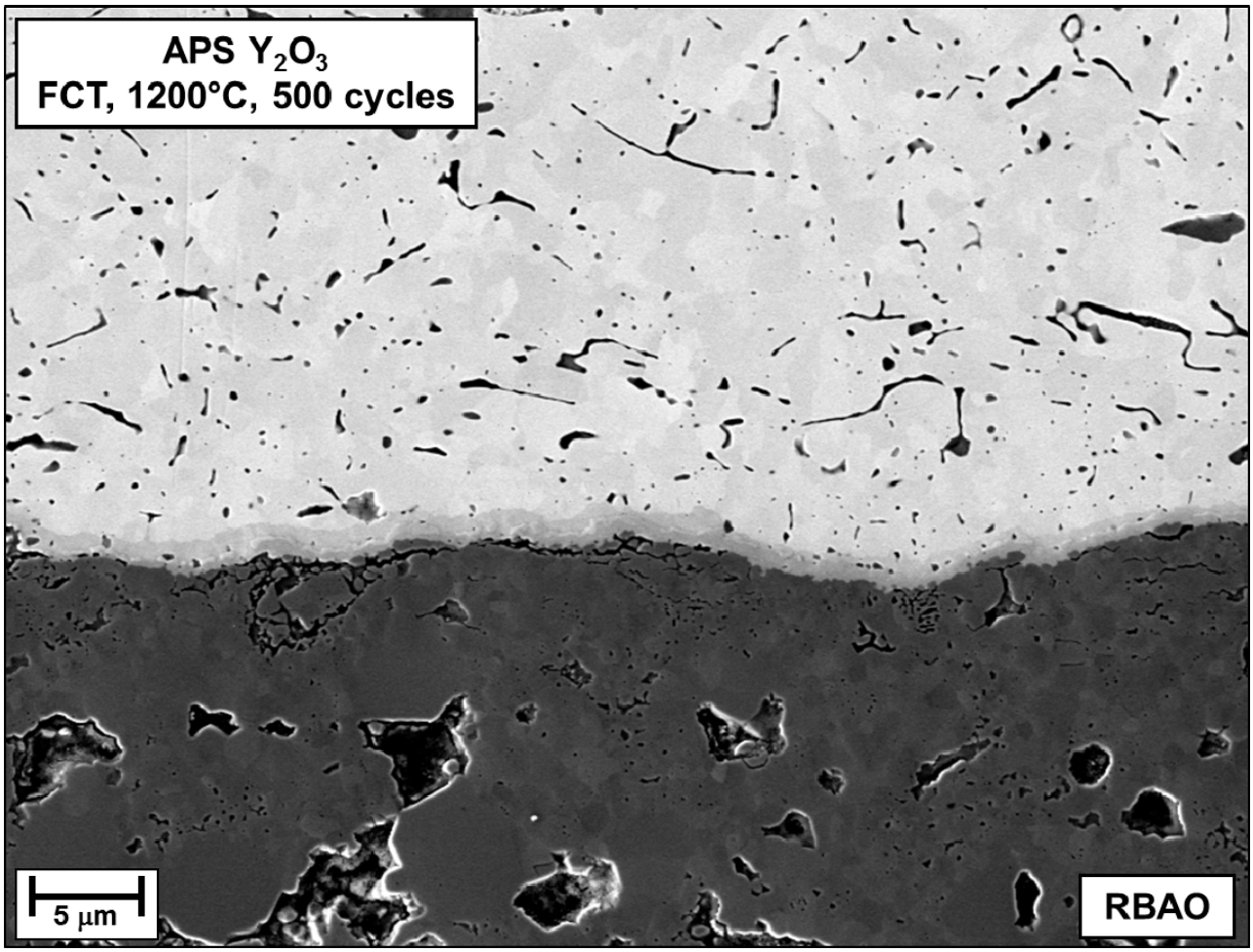

Figure 14

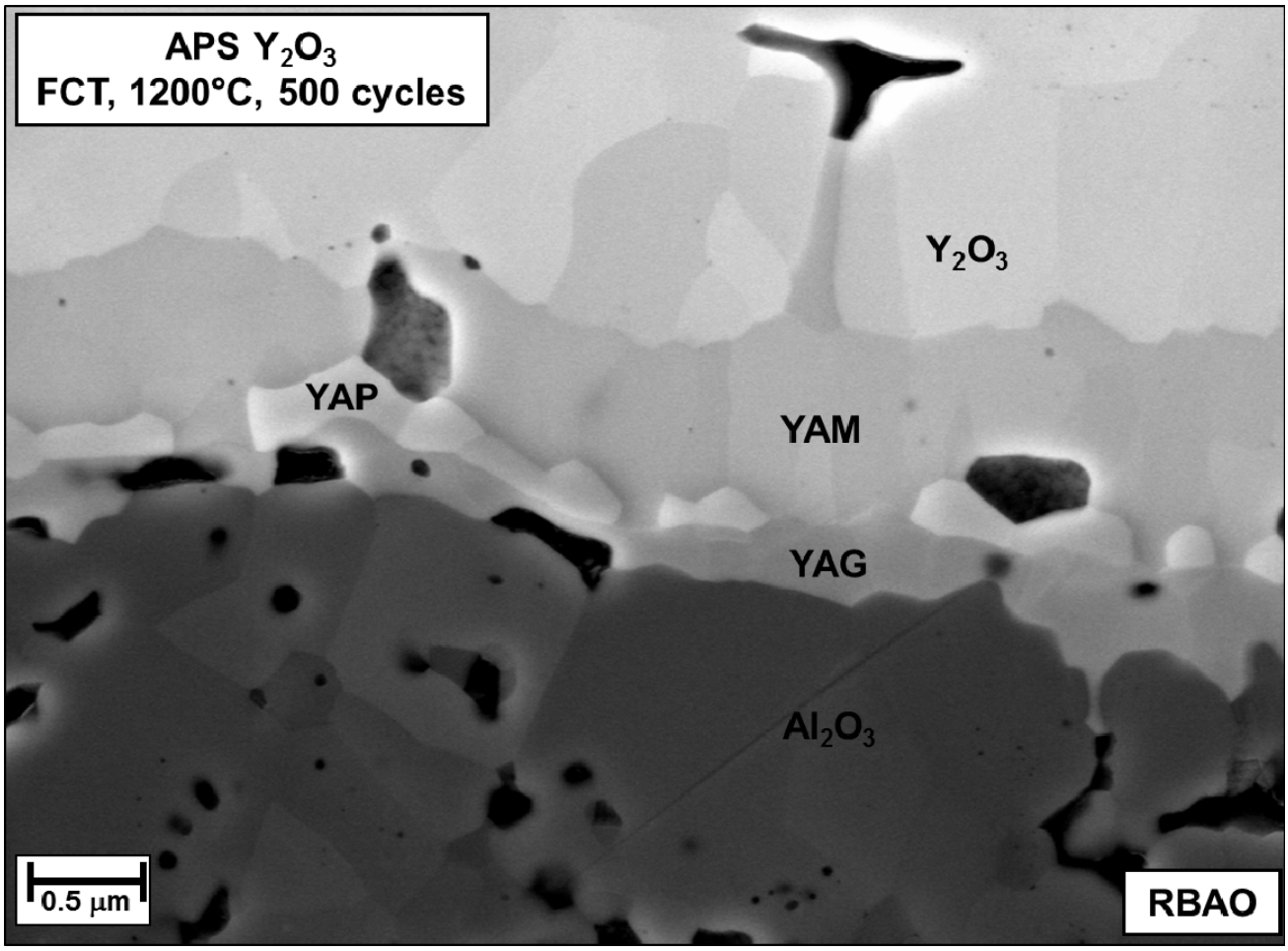
APS Y_2O_3
FCT, 1200°C, 500 cycles
Y_2O_3
YAP
YAM
YAG
Al_2O_3
0.5 µm
RBAO